



The topographic signature of temperature controlled rheological transitions in accretionary prism

Sepideh Pajang^{1,2}, Laetitia Le Pourhiet¹, and Nadaya Cubas¹

¹Institut des Sciences de la Terre Paris, ISTeP UMR 7193, Sorbonne Universite, CNRS-INSU, 75005 Paris, France

²Geoscience department, University of Birjand, Birjand, Iran

Correspondence: sepideh.pajang@sorbonne-universite.fr

Abstract. The local topographic slope of the accretionary prism is often used together with the critical taper theory to determine the effective friction on subduction megathrust. In this context, extremely small topographic slopes associated with extremely low effective basal friction ($\mu \leq 0.05$) can be interpreted either as seismically locked portions of megathrust, which deforms episodically at dynamic slip rates or as a viscously creeping décollement. Existing mechanical models of the long-term evolution of accretionary prism, sandbox models, and numerical simulations alike, generally do not account for heat conservation nor for temperature dependant rheological transitions. Here, we solve for advection-diffusion of heat with imposed constant heat flow at the base of the model domain. This allows the temperature to increase with burial, and therefore to capture how the brittle-ductile transition and dehydration reactions within the décollement affect the dynamic of the accretionary prism and its topography. We investigate the effect of basal heat flow, shear heating, thermal blanketing by sediments, the thickness of the incoming sediments. We find that while reduction of the friction during dewatering reactions result as expected in a flat segment often in the fore-arc, the brittle-ductile transition result unexpectedly in a local increase of topographic slope. We show that this counter-intuitive backproduct of the numerical simulation can be explained and by the onset of internal ductile deformation in between the active thrusts. Our models, therefore, implies significant viscous deformation of sediments above a brittle décollement, at geological rates, and we discuss its consequences in term of interpretation of coupling ratios at subduction megathrust. We also find that, with increasing burial and ductile deformation, the internal brittle deformation tends to be accommodated by backthrusts until the basal temperature becomes sufficient to form a viscous channel, parallel to the décollement, which serves as root to a major splay fault and its back-thrust and delimits a region with small topographic slope. Morphologic resemblances of the brittle-ductile and ductile segments with fore-arc high and fore-arc basins of accretionary active margins respectively allow us to propose an alternative metamorphic origin of the fore-arc crust in this context.

20 1 Introduction

Several studies have suggested a link between the morphology of fore-arc wedges and the seismic behavior of megathrusts, showing a correlation between large subduction earthquakes and fore-arc basins or deep-sea terraces (Wells et al., 2003) or with negative free-air gravity anomalies (Song and Simons, 2003; Wells et al., 2003).



Fore-arc wedges are to the first order well described by the critical taper theory (CTT) (Davis et al., 1983; Dahlen et al., 1984). This theory assumes that wedges are built by accretion of material equivalent to sand pushed by a moving bulldozer over a frictional basal décollement. This theory has been very successful in describing the equilibrium morphology of wedges in response to accretion and as a function of its effective internal and basal frictional strength (Davis et al., 1983; Dahlen et al., 1984).

The relationship between the fore-arc wedge morphology and the seismogenic behavior has been attributed to spatial variations of basal shear strength (Song and Simons, 2003) and fore-arc basins are generally associated with an extremely low effective friction along the seismogenic zone ($\mu \leq 0.05$) (Cubas et al., 2013; Pajang et al., 2021), which is also supported by heat flow measurements and thermal modeling (Gao and Wang, 2014).

The effective friction $\mu_{eff} = \tau^* / (\sigma_n)$ is the ratio of the effective shear stress τ^* to the normal stress σ_n acting on a specific plane. Effective shear stress is the shear stress τ corrected from isotropic fluid pressure contribution P_f following $\tau^* = \tau - P_f$ (Terzaghi, 1925). Effective friction differs from the internal friction of rocks $\mu = \tau / \sigma_n$, which is constant for most geological material except mineralogical clays (Byerlee, 1978). Clay minerals are hydrated phyllosilicates, which stability field is controlled mainly by temperature. Prograde metamorphic reactions that affect clay minerals release water in the system, which is suspected to raise fluid pressure and diminish effective friction. Clay contents, their nature, and their evolution during accretion may therefore affect the effective friction of the décollement as a function of temperature history.

Several studies have related the depth-dependence of subduction megathrust seismicity to the diagenetic transformation of smectite to illite, two clay minerals (Vrolijk, 1990; Hyndman et al., 1995; Oleskevich et al., 1999; Moore and Saffer, 2001).

This transition appears at $\sim 2.5 - 5$ km depth or $100 - 150^\circ C$ temperature threshold in clay-rich accretionary complexes (Pytte and Reynolds, 1988; Hyndman et al., 1995; Oleskevich et al., 1999), and could account for up to 80 percent of the excess in pore fluid pressure (Bekins et al., 1994; Lanson et al., 2009) necessary to explain the low topographic slope of fore-arc basins according to CTT. This transition is found to roughly correlate with the up-dip limit of the seismogenic zone (Oleskevich et al., 1999). Yet, the relationships between fore-arc basins and seismogenic zones do not work along all subduction zones (Song and Simons, 2003; Wells et al., 2003).

An alternative explanation for the flat slope of fore-arc basins could be the presence of a weak viscous décollement. This hypothesis is supported by rock records in exhumed large accretionary complex (Raimbourg et al., 2014; Chen et al., 2018), which show that the increase in temperature with burial permits to reach the brittle-ductile transition. Yet, this transition from solid (rate independent or rate weakening) versus fluid (rate hardening) friction is hard to parametrize within the CTT as it produces rate dependent effective friction and rate dependence is absent of CTT. Long-term models which include the tectonic and thermal structure inherited from building the fore-arc wedge are thus needed to explore alternative or reconciling explanations.

The evolution and distribution of long-term internal deformation of fore-arc wedges has been intensively studied by numerical models in two (Burbidge and Braun, 2002; Strayer et al., 2001; Buitter et al., 2016; Stockmal et al., 2007; Miyakawa et al., 2010; Simpson, 2011; Ruh et al., 2012; Ruh, 2020) and three dimensions (Braun and Yamato, 2010; Ruh et al., 2013; Ruh, 2016) complementing analogue models (see (Graveleau et al., 2012) for a review). While these models have covered



the influence of many parameters such as the geometry (Dahlen et al., 1984; Davis et al., 1983; Koyi and Vendeville, 2003; Mandal et al., 1997; Smit et al., 2003; Ruh et al., 2016), basal friction (Colletta et al., 1991; Lallemand et al., 1994; Mulugeta, 1988; Nieuwland et al., 2000; Burbidge and Braun, 2002; Ruh et al., 2012; Cubas et al., 2008), surface processes e.g., (Storti and McClay, 1995; Mary et al., 2013; Willett, 1999; Leturmy et al., 2000; Konstantinovskaya and Malavieille, 2005; Bonnet et al., 2007; Fillon et al., 2013; Mary et al., 2013; Stockmal et al., 2007; Hoth et al., 2006; Simpson, 2006), or the presence of viscous material along the décollement (Gutscher et al., 2001; Costa and Vendeville, 2002; Smit et al., 2003; Couzens-Schultz et al., 2003; Bonini, 2007; Pichot and Nalpas, 2009; Simpson et al., 2010; Ruh et al., 2012; Yamato et al., 2011; Borderie et al., 2018). Despite the large amount of published studies, none of them included the dependence of effective basal friction on temperature due to metamorphic reaction or brittle-ductile transition.

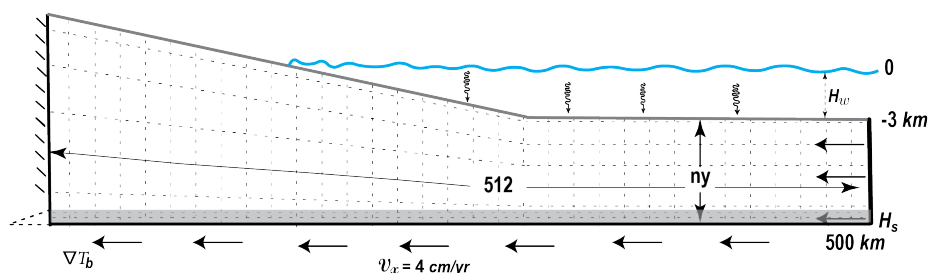


Figure 1. Model set-up. Mechanical boundary conditions are a non-deformable backstop on the left side, a constant velocity in the horizontal direction of $4 \text{ cm} \cdot \text{year}^{-1}$, the top boundary behaves as a free surface above sea level while the weight of the water column is prescribed as stress normal to the deformed boundary below sea level. Temperature is fixed at the surface, the thermal gradient is prescribed across all other boundaries with the value of zero on vertical ones and value of ∇T_b at the bottom boundary. The mesh consists of $512 \times ny$ Q2P1 elements which deform to adapt to the deforming top boundary. Parameters are defined in Table 1.

Here, we study how the introduction temperature evolution and its feedback on rock rheology generates deviations from CTT. For that purpose, we use a typical CTT set up (Figure 1) and we solve for the heat equation on the same domain with a constant heat flow boundary condition at the base, which corresponds to plate age, to allow the temperature to increase with burial. As this contribution focuses on the thermal effect, we also include shear heating and thermal blanketing of sediments. We present different series of 2D thermo-mechanical simulations which assess how the brittle-ductile and the smectite-illite transitions affect the topographic slope of an accretionary prism and its internal deformation. We briefly discuss internal deformation the morphology of the wedge and its potential seismic behavior. We, therefore, retrieve the spatial and temporal variation of the morphologies and deformation patterns and discuss their implications in terms of the fore-arc basin and fore-arc high genesis and nature.



2 Modelling Approach

2.1 Method

In order to model the long-term behavior of the accretionary prism, we use pTatin2d (May et al., 2014, 2015), a code based on finite element method that employs an arbitrary Lagrangian-Eulerian (ALE) discretization together with the material point method to solve the conservation of momentum (Eq. 1), mass (Eq. 2) and energy (Eq. 3) for an incompressible fluid. It allows solving thermo-mechanical problems. It has been widely used to model lithospheric scale long-term tectonic problems coupled to surface processes (Jourdon et al., 2018; Perron et al., 2021) and benchmarked with sandbox experiments (Buitter et al., 2016).

The code solves for velocity v and pressure P assuming conservation of momentum:

$$\nabla \cdot (2\eta\dot{\epsilon}) - \nabla P = \rho\mathbf{g}, \quad (1)$$

in an incompressible fluid assuming

$$\nabla \cdot \mathbf{v} = 0, \quad (2)$$

of nonlinear effective viscosity η and constant density ρ . $\dot{\epsilon}$ is the strain rate tensor and \mathbf{g} the gravity acceleration. Evolution of temperature T is obtained by solving the time, t , dependent conservation of heat,

$$\frac{\partial T}{\partial t} = \nabla \cdot (\kappa\nabla T) - v\nabla T + \frac{H}{\rho C_p}. \quad (3)$$

The coefficients of eq.3 are κ the thermal diffusivity, C_p the heat capacity, and H the heat production. We do not include radiogenic heat production in our simulation and

$$H = 2\eta(\epsilon_{xx}^2 + 2\epsilon_{xy}^2 + \epsilon_{yy}^2) \quad (4)$$

corresponds to the sole shear heating.

The Stokes problem eqs. 1 and 2 is solved using high order stable elements (Q₂-P₁), while the heat equation eq.3 is discretized on Q₁ elements. Physical properties of rocks are computed on Lagrangian markers and projected to gauss points using constant value per element. Averaging of marker-defined coefficients within element is geometric for viscosity and algebraic for other properties. At every time step, the surface of the models, h , is smoothed according to the Culling diffusive erosion law,

$$\frac{\partial h}{\partial t} = -\nabla \cdot (k\nabla h) \quad (5)$$

with a diffusion coefficient k . Details on implementation of the surface process model in pTatin2d are to be found in (Jourdon et al., 2018).



2.2 Rheological model

We use temperature and pressure-dependent nonlinear rheologies. Effective viscosity is evaluated on material points using first
105 the Arrhenius flow law for dislocation creep,

$$\eta_{vis} = A^{-\frac{1}{n}} (\dot{\varepsilon}^{\text{II}})^{\frac{1}{n-1}} \exp\left(\frac{Q + PV}{nRT}\right) \quad (6)$$

written in term of the second invariant of the strain rate tensor $\dot{\varepsilon}^{\text{II}}$. The activation volume is set to $V = 8 \times 10^{-6} \text{ m}^3 \cdot \text{mol}^{-1}$ for all the lithologies, the other constants A, n, Q are listed for each lithology in Table 1. If the prediction of the second invariant of stress for a viscous rheology

$$110 \quad \sigma^{\text{II}} = 2\eta_{vis}\dot{\varepsilon}^{\text{II}} \quad (7)$$

exceeds the Drucker-Prager frictional plastic yield criterion,

$$\sigma_Y = \sin \phi P + C \cos \phi \quad (8)$$

which depends on ϕ the internal friction angle and C the cohesion, the effective viscosity of the marker is corrected in order to return to the yield envelop with

$$115 \quad \eta_p = \frac{\sigma_Y}{2\dot{\varepsilon}^{\text{II}}} \quad (9)$$

Finally, the friction angle ϕ and cohesion C decrease linearly with accumulation of strain in the plastic regime ε_p from an initial friction ϕ_0 to a final friction ϕ_∞ (resp. C_0 and C_∞ for cohesion):

$$\phi = \phi_0 - \frac{\varepsilon_p - \varepsilon_{\min}}{\varepsilon_{\max} - \varepsilon_{\min}} (\phi_0 - \phi_\infty), \quad (10)$$

over a range of accumulated plastic strain varying from $\varepsilon_{\min} = 0$ to $\varepsilon_{\max} = 0.5$. This drop of friction and cohesion does not
120 apply to the décollement. Frictional parameters are listed together with viscous parameters, density, and thermal diffusivity in Table 1. As all stokes solvers, pTatin2d also applies cut-off values on effective viscosity in order to maintain a reasonably well-conditioned system of equations. These are set to a minimum value $\eta_{\min} = 10^{16} \text{ Pa}\cdot\text{s}$ and a maximum value $\eta_{\max} = 10^{25} \text{ Pa}\cdot\text{s}$. We made sure that the minimum is never reached to ensure that the frictional properties of the décollement reflect its extremely low friction.

125 2.3 Initial and Boundary Conditions

The model domain is 500 km long and its initial thickness is either 4 or 7.5 km (Figure 1). It is constituted of 2 layers, a 500 m thick décollement modeled by shales, while the rest is modeled by sandstones/quartz. The domain is discretized with a mesh of 512×16 and 512×24 Q2 elements, respectively. In the y-direction, two mesh elements are aligned with the initial décollement layer to better capture its interface and friction at small strain. The décollement material is considered as part of the domain,
130 as such, we allow shales to be dragged in the rest of the model domain contrarily to frictional boundary conditions adopted



Parameter	Name	Unit	Sandstone/Quartz ^a	Shale ^b	Sediment/quartz ^a
A	Pre-exponential factor	MPa ⁻ⁿ .s ⁻¹	6.8 × 10 ⁻⁶	1.3 × 10 ⁻⁶⁷	6.8 × 10 ⁻⁶
n	Exponential stress	-	3	31	3
Q	Activation energy	kJ	156	98	156
C ₀	Initial cohesion	MPa	2	0.1	2
C _∞	Final Cohesion	MPa	1	0.1	1
φ ₀	Initial friction	°	25	5	25
φ _∞	Final friction	°	10	5*	10
κ	Heat diffusivity	m ² .s ⁻¹	10 ⁻⁶	10 ⁻⁶	10 ⁻⁷
ρ	Density	kg.m ⁻³	2400	2400	2000

Table 1. Variable rheological parameters and coefficients for the different lithologies; creep parameters ^a from (Ranalli and Murphy, 1987) and ^b from (Shea and Kronenberg, 1992). * In models **M13** to **M15** the friction in the Shale is temperature dependent.

to benchmark the code with sandbox experiments (Buiter et al., 2016). The shortening of the model is driven by a constant horizontal velocity $v_x = 4\text{cm/yr}$ applied both at the right and bottom boundaries. Above the décollement level, the left side of the domain is rigid. Within the 2 mesh elements of the left boundary which belongs to the décollement, a vertical velocity gradient is applied to ensure the continuity with the bottom boundary. The surface of the domain is modeled with a free surface
 135 above sea level (located 3 km above the top of the mechanical model, Figure 1), below sea level additional normal stress:

$$\sigma_n = H_w \rho_w g \quad (11)$$

is applied on the deformed surface to mimic the weight of water, yet shear stress is zero like above sea level.

The thermal boundary conditions assign the temperature $T_0 = 0^\circ\text{C}$ at the surface, a constant thermal gradient $\nabla T_b = \frac{\partial T}{\partial y} \Big|_{y=y_b}$ at the base and no horizontal gradient/(insulating boundary) on the vertical walls of the domain. As we assume
 140 no radiogenic heat production, the initial temperature in the domain is fixed to:

$$T = T_0 - \nabla T_b y \quad (12)$$

consistently with the boundary conditions.

2.4 Post-processing

Models are named by a number within a bullet on the left of the panels. This number refers to Table 2 which contains all the
 145 specific parameters used for this realization of the model. For each simulation, we show the finite strain and the current state and strain rate.

The finite strain figure displays the lithologies of rocks and the accumulated plastic strain on markers with a linear colormap. Markers with values of plastic strain ε_p larger than 2 or 3 can be interpreted as being part of a fault. In order to better show the deformation, sandstone sequences have been colored with thin layers that have no physical existence. Sediment markers
 150 deposited by surface processes are colored by the time of deposition from brown to yellow colors.



The current state figure displays whether the material is yielding plastically (blue) or deforms viscously (red). It is overlaid by green shades of the second invariant of strain rate to outline structures that are currently active by comparison to finite strain. A cut-off range from $5 \times 10^{-16} s^{-1}$ to $2 \times 10^{-14} s^{-1}$ is used for the post-processing. The actual values span a larger range. We also represent three isotherms (180, 300, and $450^{\circ}C$) which have been chosen to correspond to the onset of viscous deformation in low strain islands, brittle-ductile transition for quartz at average strain-rate and completely ductile behavior. In the simulation with dehydration reactions, the $120^{\circ}C$ isotherm is added to locate the onset of the dehydration reaction. Finally, we represent the local slope with a color code at the top of the slice.

2.5 Experimental plan

Model	H_s (km)	n_y	∇T_b ($^{\circ}C/km$)	k	SH	DR
M0	4	16	-	10^{-6}	off	off
M1	4	16	15	10^{-6}	on	off
M2	4	16	15	10^{-6}	off	off
M3	4	16	15	10^{-5}	on	off
M4	4	16	15	10^{-5}	off	off
M5	7.5	24	15	10^{-6}	off	off
M6	7.5	24	15	10^{-5}	off	off
M7	7.5	24	15	10^{-6}	on	off
M8	7.5	24	15	10^{-5}	on	off
M9	4	16	25	10^{-6}	on	off
M10	4	16	25	10^{-5}	on	off
M11	7.5	24	25	10^{-6}	on	off
M12	7.5	24	25	10^{-5}	on	off
M13	4	16	15	10^{-6}	off	on 5-0.1-10
M14	4	16	15	10^{-6}	on	on 5-0.1-10
M15	4	16	15	10^{-6}	on	on 5-0.1-5

Table 2. Variable parameters. H_s = Domain thickness, n_y = Number of vertical element, ∇T_b = basal thermal gradient, k = coefficient of diffusion for surface process model, SH = Shear heating, DR=Dehydration reaction followed by values for temperature dependant internal friction angle in $^{\circ}$.

Our aim is to provide the community with a first assessment of the topographic expression of the change in thermo-rheological regime with burial in an accretionary prism. We, therefore, have chosen a simple reference model which produces well defined thrust and back thrust, with a moderate amount of sedimentation. The effects of softening, basal friction, and basal slope on accretion have already been thoroughly studied e.g., (Graveleau et al., 2012; Buitter et al., 2016; Ruh et al., 2012, 2014).



Hence, we here concentrate on parameters that are known to affect the geotherm: basal heat flow (represented by basal thermal gradient ∇T_b), initial burial (H_s), coefficient of diffusion of the topography (erosion and sedimentation) (k), and shear heating (SH) following the plan listed in Table 2. In all the experiments, thermal blanketing (Jeffreys, 1931; Wangen, 1994) is very roughly simulated by using a lower thermal diffusivity for sediments produced by the surface process model (see Table 1). As we do not simulate the compaction of sediments with burial, thermal insulation is probably over-estimated but it allows testing potential effects of sedimentation on the thermal state of the accretionary wedges.

170 3 Main Results

3.1 Effect of brittle-ductile transition at one glance

In Figure 2, we first compare the results of our reference model (**M1**), with a 4 km thick pile of sediments affected by moderate erosion sedimentation, shear heating, and a thermal gradient of $15^\circ/\text{km}$ which corresponds to a plate age of 65Ma, with the same model run without thermal coupling (**M0**).

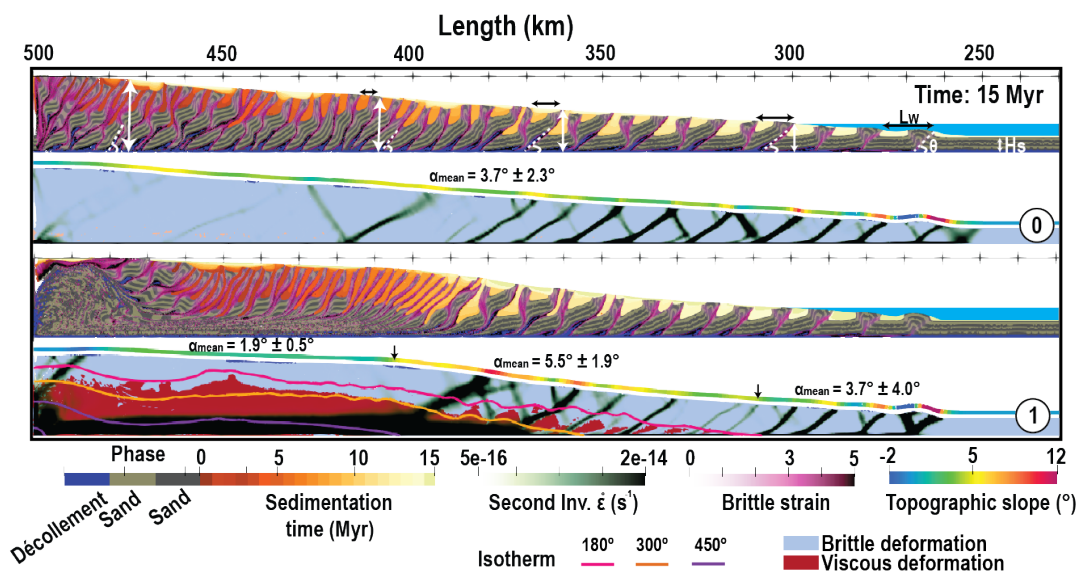


Figure 2. Model M0: without temperature compared to **Model M1:** the same experiment with temperature dependant rheologies, both after 15 Myr evolution. The finite strain and the current state and strain rate are shown for basal frictional angle ($\phi_b=5^\circ$) and internal friction angle dropping from 25° to 10° with strain. The yellowish-brown color illustrates syn-tectonic sedimentation in the form of piggyback basins which represent a given age that corresponds to the time of deposition. Where the material is yielding plastically is in blue or deforms viscously is in red with the onset of 180, 300, and 450°C isotherms. Black arrows display decreasing thrust space towards the backstop and white arrows show increasing sequence thickness and inclination angle θ . The local topographic slope with a color code shown at the top of the slice is affected by temperature and frictional properties.



175 While the frontal parts are not significantly different, with similar tapers and ramp spacing, as soon as the thickness of the wedge doubles (close to sea level at x c.a. 300 km), the back-thrusts are more active in the purely brittle wedge than in the thermally controlled wedge for these brittle parameters. This results in the deactivation of one ramp over two, which leads to the formation of the distinct twinned-slice patterns observed between $x = 430$ km and $x = 300$ km in **M0**. In **M1**, the twinning of slice by back thrust occurs only once the temperature at the base of the model reaches 300°C .

180 Looking at the internal part of the two accretionary prisms, the differences become of course more striking. In the case without thermal coupling (**M0**), deformation continues by pairing together more and more slices within sequences of thrust and back-thrust which root deeper and deeper as the accretionary prism thickens. The prolonged activity of these out-of-sequence thrusts and back thrust is best measured by the small out-of-sequence basins that form at their top, discordant on the older sediments. Very little exhumation occurs close to the back-stop. In the case of thermal coupling, as soon as the 450°C
185 isotherm is reached, deformation becomes highly partitioned vertically. A thick layer at the base accommodates the simple shear and branches on main frontal thrusts which root at the brittle-ductile transition. The ductile material is exhumed along a normal fault that roots on the backstop. In between, the deformation in the brittle part is either very distributed or almost nonexistent as the strain rate remains below our visualization threshold.

In the end, zooming out of these details and looking at the topographic slope, we can see that while the brittle accretionary
190 wedge displays a rather constant 4° slope, as predicted by the CTT taking into account the softening parameter (Ruh et al., 2014), the mature brittle-ductile wedge forms three distinct segments with a rather low but non zero topographic slope close to the backstop, a CTT predicted slope close to the toe of the wedge and in between a zone with a distinctively larger topographic slope which corresponds to the brittle-ductile transition.

3.2 From the emergence of the transition slope to steady state wedge

195 Figure 3 shows the structural evolution of the reference simulation **M1** through time. The wedge grows horizontally by in-sequence thrusting and vertically by reactivation of thrusts within the wedge. Most of the horizontal shortening is accommodated by the active frontal thrust. As the wedge evolves, the surface slope also changes and we detail here its evolution in time.

After 1 Myr, accumulated plastic strain shows that the deformation is strongly localized along the frontal part and on the
200 décollement. Shear bands initially occurred in conjugate sets; with ongoing shortening, landward dipping shear zones are preferred and back-thrusts are almost abandoned. The wedge is trying to reach a critical state by creating a topographic slope. Due to internal frictional softening, the brittle wedge present a slope $\bar{\alpha}$, which corresponds to the slope predicted by CTT for basal friction ϕ_b and internal friction of 17° , i.e. the average of $\phi_{\infty} = 10^{\circ}$ and $\phi_0 = 25^{\circ}$.

At 5 Myr, some patches of viscous deformation appear in between the main faults at $x = 413$ km once the base of the model
205 reaches 180°C . From that point, landward plastic strain and the second invariant of the strain rate indicate the activity of out-of-sequence thrusts and steep back-thrusts which dissect the former slices and tend to flatten horizontally the sequences as the former ramps become more and more vertical. This phenomena induces vertical thickening that correlates with the occurrence of internal viscous deformation at depth and with an increase in local slope $\bar{\alpha}$ independently of basal friction which remains

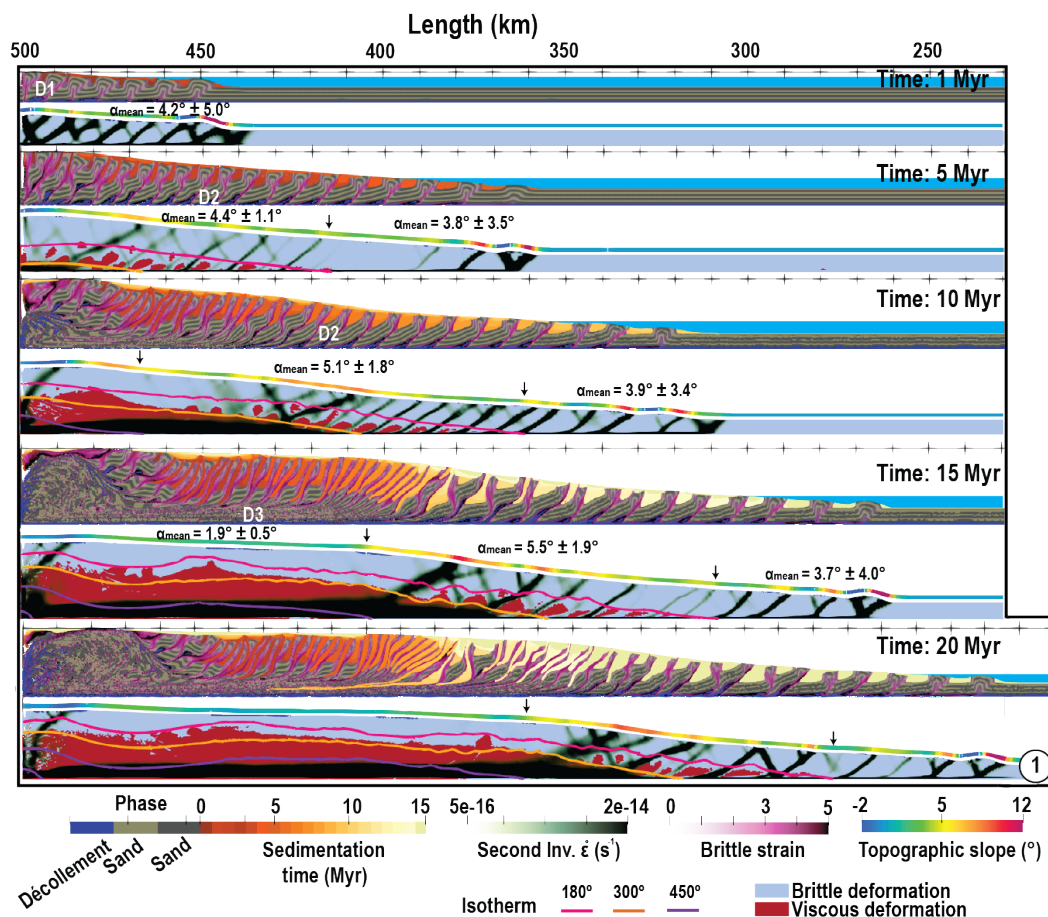


Figure 3. Temporal evolution of the reference model (M1) from beginning to 20 Myr of shortening.

constant. This increase in slope causes an increase in sedimentation rate at the front where piggyback basins tend to be more
 210 starved than in the initial phase favoring the activity of thrusts, and a lengthening of the slices as predicted by other studies like
 Storti and McClay (1995) using sandbox experiments or Simpson et al. (2010) using numerical simulations.

As the shortening goes on, the temperature continues increasing at the back of the wedge due to burial. Between 5 and 10
 Myr, the strain rate shows that the thickness of the décollement increases to reach 2 km. A normal fault forms near the backstop
 and starts accommodating the exhumation of high metamorphic grade rocks, which deforms in a ductile manner. At the front
 215 of this wide ductile horizontal shear zone, which terminates right at the 300°C isotherm, roots a system of low angle thrusts
 and high angle backthrusts which separates the warm distributed part of the wedge from the thrust dominated section of the
 wedge.

From 10 to 15 Myr, the warm part of the wedge grows in length and its topography flattens. The vertical partitioning
 between simple shear at the base and pure shear at the top becomes evident. At the front of this ductile wedge, the transition



220 zone, where thrusts and their back-thrust roots directly in the ductile décollement near the 300°C isotherm, develops giving rise to a distinctively larger slope than predicted by CTT. At the toe of the wedge, the slope remains constant and CTT compatible.

At 20 Myr, the overall architecture of the accretionary prism has not changed, the whole wedge is just shifted towards the right as the ductile part of the wedge has grown wider. One could state that the brittle-ductile wedge has reached some sort of steady state between 10 and 15 Myr. Rocks that are incorporated in the wedge start by rotating along with brittle thrust and
 225 maybe deforming in a pure brittle manner within the slice. In a second semi-brittle phase, internal viscous-ductile deformation affects the whole tectonic slices separated by brittle thrusts. This phase corresponds to crossing the zone with a higher than normal topographic slope. Finally, depending on whether they were incorporated in the ramp or not, they go through passive rotation by distributed pure shear thickening associated with low temperature or intense ductile simple shear before being exhumed for large temperature.

230 In conclusion, the large slope segment which corresponds to the brittle-ductile transition is acquired as soon as some viscous internal deformation occurs in between faults. The brittle-ductile wedge reaches a steady state when ductile deformation becomes predominant on the décollement that is for temperature greater than 450°C.

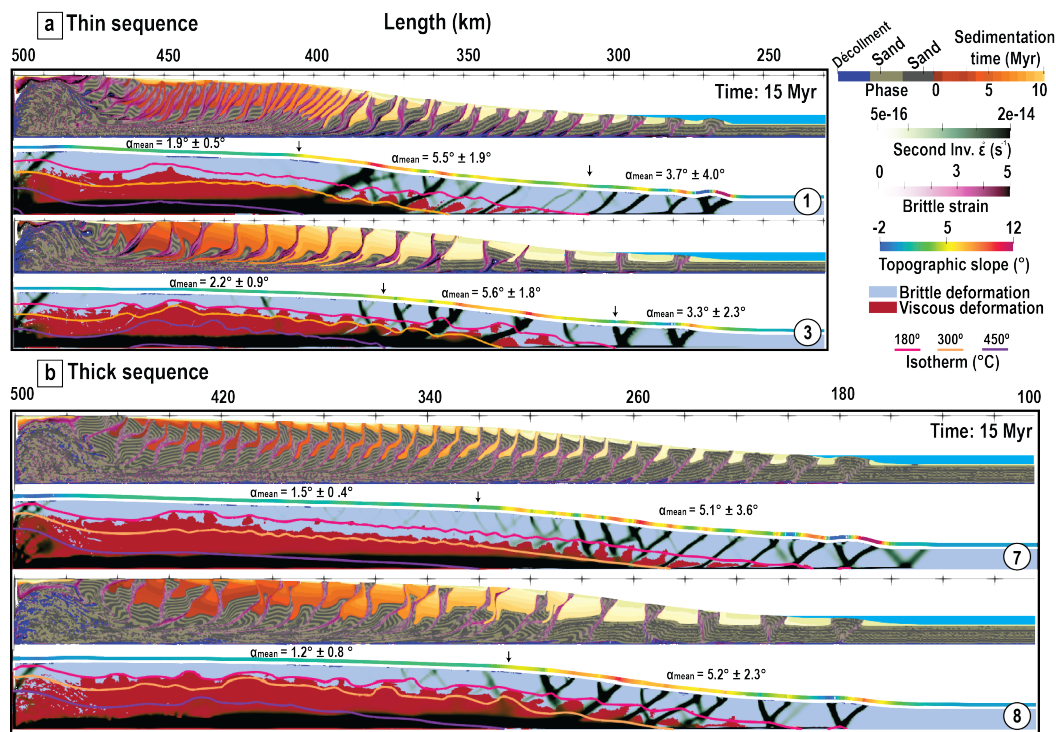


Figure 4. Models with shear heating on after 15 Myr of shortening. **a.** Thin and **b.** Thick sequence pile models. **M1, M3** and **M7, M8** are the same experiment with normal and high sedimentation rate respectively. Experiment parameters are given in Tables 1 and 2 and color code for markers is given in Figure 2.



3.3 Sensitivity Analysis

Depending on the chosen thermal parameters, the three segments described above are more or less developed in our simulations. A major player in the development of the ductile flat part of the wedge associated with high grade metamorphic rock exhumation and formation of a forearc basin is the occurrence of shear heating.

Shear heating might be largely reduced by several factors and noteworthy enough the presence of water which reduces the ductile strength of the material or by thermal pressurization during earthquakes (Sibson, 1973; Lachenbruch and Sass, 1980; Mase and Smith, 1984, 1987; Segall and Rice, 2006). Gao and Wang (2014) actually showed that megathrusts that produce great earthquakes tend to dissipate less heat than megathrusts that slip mainly by creep. Hence, our shear heating models give a maximum bound for the heat that could be produced in the system. In order to study the other bound, we ran some model with shear heating off which would correspond to a system where most slip is accommodated by earthquakes.

Results are clear, all models with shear heating (Figure 4) develop a large flat area because the shear at depth helps the temperature to rise above the 450°C isotherm, which correlates with the formation of the topographic plateau where high grade metamorphic rocks are exhumed. Models with no shear heating hardly develop a plateau and a normal fault to exhume high grade material at the back (Figure 5).

Actually, only models with large erosion coefficients, i.e. **M4** and **M6**, do produce exhumation and a small plateau when shear heating is deactivated. The peak metamorphic temperature of rocks exhumed at the back-stop in presence of shear heating or in models with large erosion rate is compatible with thermochronometry studies in stationary accretionary prism like Taiwan (Suppe et al., 1981; Willett and Brandon, 2002) which indicate the samples exhumed to the surface by rock uplift to compensate for the mass lost by erosion (Fuller et al., 2006) have experienced temperatures in excess of $300\text{--}365^{\circ}\text{C}$ but below 440°C e.g., (Lo and Onstott, 1995; Fuller et al., 2006).

Models with larger sedimentation rate (models **M3**, **M4**, **M6**, **M8**, **M10**, **M12**) produce, as expected from former studies (Storti and McClay, 1995; Simpson et al., 2010), a smaller number of thrusts and a larger spacing between them. Erosion and sedimentation also participate at reducing the slope at every step, thus favoring out-of-sequence activity (Figure 5 **M2** and **M4**). In our models, sediments also affect the thermal regime because they are attributed a lower thermal diffusivity; thick sediment sequences act therefore as a blanket isolating the heat flux coming from below. As a result, temperature raises faster at depth when large sedimentary basin forms. This explains why, in absence of shear heating (Figure 5), only models with large sedimentation rate develop a ductile flat at the back (Figure 5 **M4** and **M6**).

Thermal blanketing also affects the geotherm at a smaller scale as shown by the distinctive wiggles in the isotherms. For small basins, these wiggles are limited to the 180°C isotherm (Figure 5 **M2** and **M5**), but for large basins the 300°C isotherm is affected at larger wavelength and potentially feeds back on the rheology (Figure 5 **M4** and **M6**).

In absence of heat production and large vertical advective terms, the temperature is more or less proportional to depth and thermal gradient in the models, experiments with thick sequences (**M5** and **M6** in Figure 5 and **M7** and **M8** in Figure 4) or larger imposed basal gradient (**M9**, **10**, **11**, **12** in Figure 6) reach the onset of brittle-ductile transition earlier. As a result, the completely brittle part of the accretionary prism, located at the toe of the wedge, is less developed in models with a larger pile

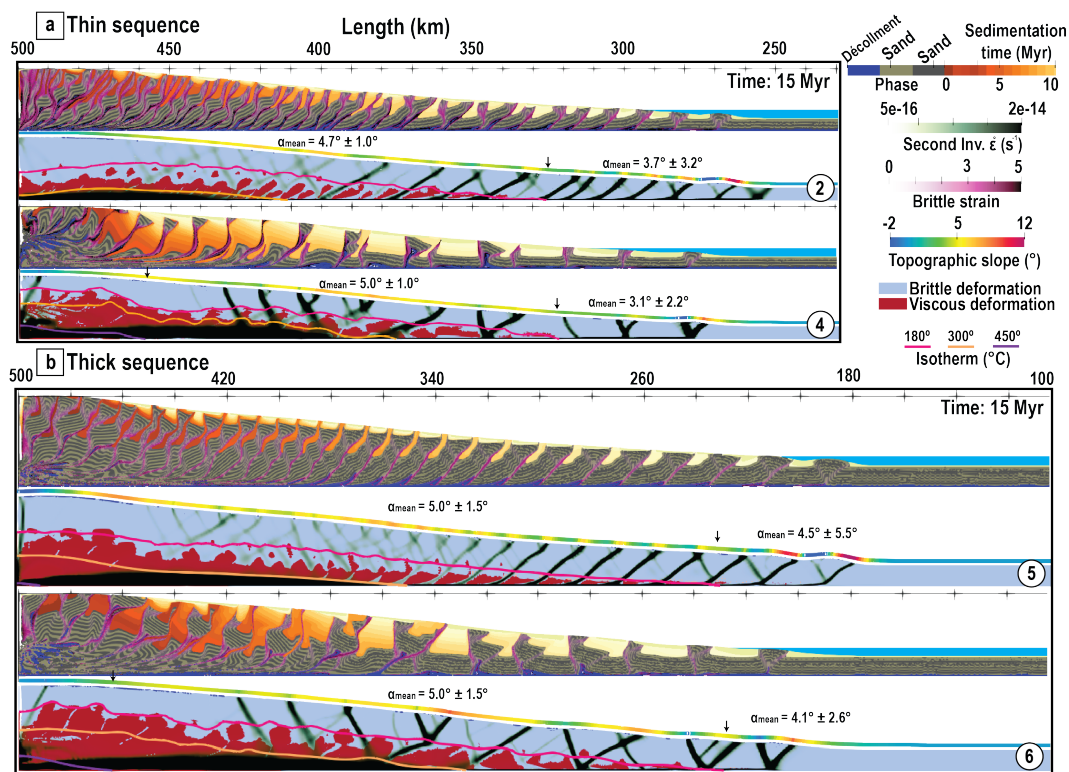


Figure 5. Models with no Shear heating after 15 Myr of shortening for **a.** Thin and **b.** Thick sequence pile models. Normal sedimentation rate use in **M2** and **M5**, and high erosion rate in **M4** and **M6**. Refer to Figure 2 for color codes and Tables 1 and 2 for experiment parameters.

of incoming sediments and in models with a larger thermal gradient. The local slope in these models is always larger than the CTT predicted one and back-thrust appear earlier in the history of deformation.

3.4 Effect of Dehydration reactions

270 We now report some models which intend to tackle the effect of fluid over pressure due to dehydration of shale materials which potentially corresponds to smectite-illite transition. In clay-rich accretionary complexes, this transition appears at $\sim 2.5 - 5$ km depth corresponding approximately to $100-150^\circ C$ (Pytte and Reynolds, 1988; Hyndman et al., 1995; Oleskevich et al., 1999). Smectite and illite clays are frictionally weak but illite is slightly stronger (Morrow et al., 1982; Saffer and Marone, 2003). We, therefore, consider that our clay rich décollement is initially smectite rich with an internal friction angle of 5° . Once
 275 dehydration reaction is terminated the same décollement is considered illite rich and affected a friction angle of 10° . We do not have a kinetic reaction included in the code but we assume that the reaction is occurring at fast rate in the $120-140^\circ C$ window. This is slightly smaller than the $100-150^\circ C$ reported in the literature and it is aimed at roughly accounting for a slow kinetic at lower temperatures and the lack of reactant (smectite) left at higher temperatures. During this phase of fast reaction, fluids

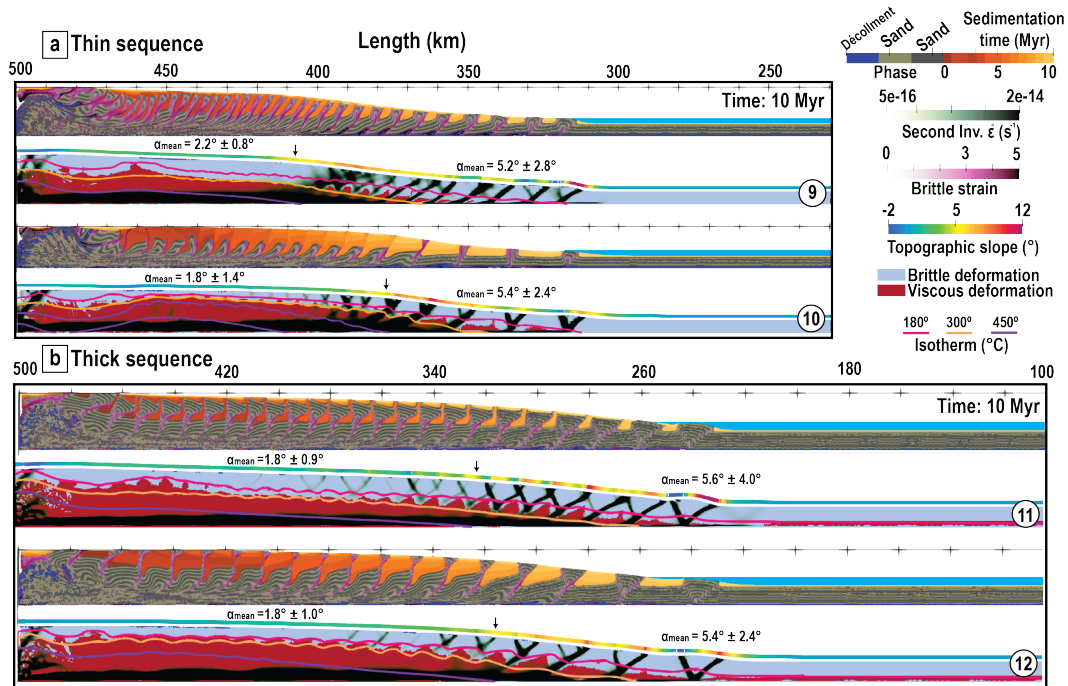


Figure 6. High temperature gradient ($25\text{ }^{\circ}\text{C}/\text{km}$) after 10 Myr for **a.** thin sequence and **b.** thick sequence. **M9** and **M11** are with normal erosion and sedimentation rate whereas **M10** and **M12** indicate high sedimentation rate. Color codes and experiment parameters are given in Figure 2 and Tables 1 and 2.

are released in the clay rich décollement of low permeability permitting to build strong local fluid over pressure (Bekins et al., 1994; Lanson et al., 2009). The code does not explicitly include fluids, but these overpressures are reflected by an effective friction angle of 0.1° within the reaction temperature window. The evolution of friction with temperature in the décollement layer is reported in Figure 7.

Figure 8 shows the structural evolution of simulation **M14**, identical to the reference model **M1** but accounting for the smectite-illite transition.

After 1 Ma, by the formation of conjugate shear bands, the wedge tries to reach its critical state in accordance with basal friction of $\phi_b = 5^{\circ}$. Since the base quickly reaches $120\text{ }^{\circ}\text{C}$, the frontal wedge is extremely narrow, and followed by a flat area induced by the drop of friction ($\phi_b = 0.1^{\circ}$), as expected from CTT.

At 3.8 Ma, the flat area is highly extended ($x = 380 - 470\text{ km}$). The onset of this transition serves as the root to a shallow splay fault accompanied by a back-thrust.

At 6.3 Ma, as the shortening goes on, the temperature rises due to burial. Once the décollement reaches $140\text{ }^{\circ}\text{C}$, the basal friction increases to 10° , leading to the onset of a larger topographic slope. Once the décollement reaches $180\text{ }^{\circ}\text{C}$, some patches of viscous deformation appear in between active thrusts (at $x = 440\text{ km}$). As observed in model **M1**, a segment of the

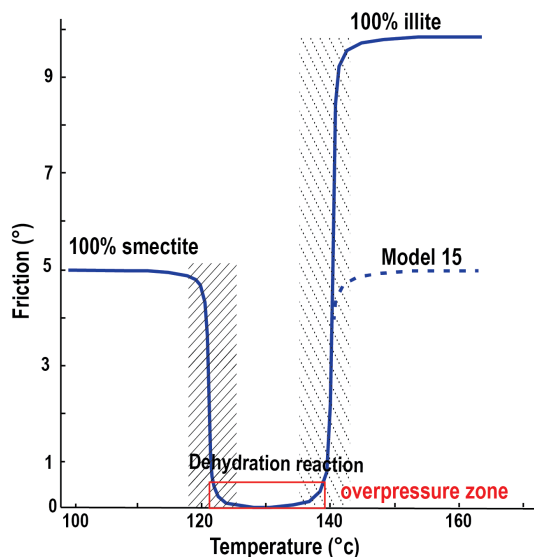


Figure 7. Evolution of friction with temperature with our parametrisation of smectite-illite transition. The dashed line is for the evolution of friction in simulation M15 which serves as comparison with M1 at the brittle-ductile transition zone.

high topographic slope, formed by a low angle thrust and its backthrusts, separates the flat segment from the warmer distributed part of the wedge.

295 At 10 Ma, the wedge is characterized by four distinct segments: a narrow frontal critical taper, a weakly deformed zone with a flat topographic slope associated with the smectite-illite transition (120 to 140 °C), a high topographic slope corresponding to the brittle-ductile transition formed by a low angle thrust and its backthrusts rooting on the ductile décollement, and, finally, a second flat segment corresponding to the ductile wedge once the décollement reaches a temperature of 450 °C. The brittle-ductile transition segment shows a larger topographic slope than the reference model **M1** (Figure 3), because of the higher basal
300 friction reached once the dehydration reaction finishes ($\phi_b = 10^\circ$). From 10 to 15 Ma, the warm and flat part of the ductile wedge grows in length like in model **M1**.

Figure 8b illustrates that shear heating tends to increase the extent of the flat dehydration segment by reducing both the size of the critical taper located at the toe of the wedge and the lateral extent of the steep segment located at the brittle-ductile transition. Figure 8c demonstrates that the increase of slope of the brittle-ductile segment in model **M14** as compared to model
305 **M1** is indeed related to the increase in basal friction up to 10° after the dehydration reaction.

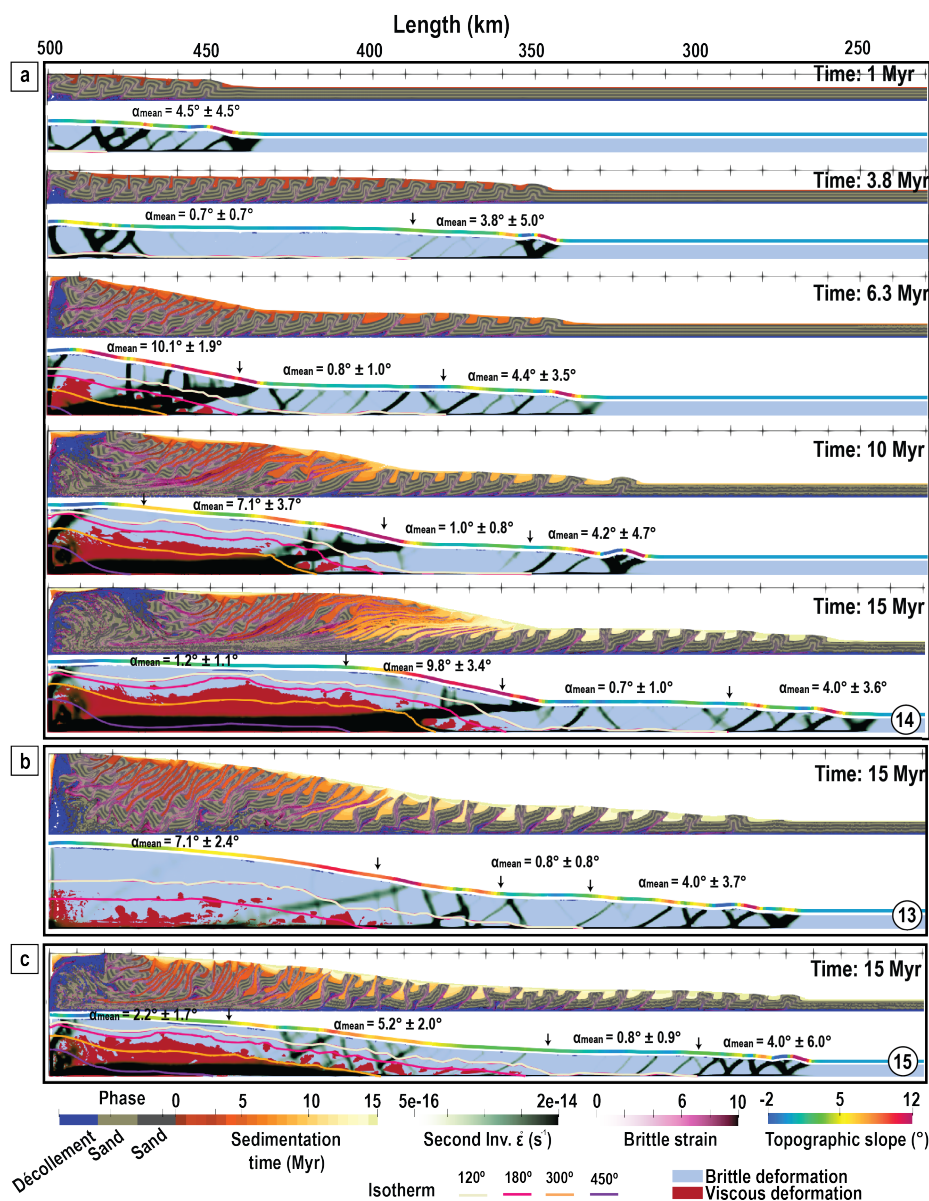


Figure 8. a. 15 Myr of time evolution of simulation *M14* with dehydration reaction and shear heating . b. cross-sections at 15 Myr for similar simulation without shear heating *M13*. c. cross-sections at 15 Myr for similar simulation *M15* with 5° friction instead of 10° friction after the end of dehydration reaction.



4 Discussion

4.1 Slopes and modes of deformation

The thermomechanical model provides an opportunity to investigate the specific variations of topographic slope of an accretionary prism, supported by the CTT analysis (Davis et al., 1983). Our results show that very simple models of accretionary prism lead to the formation of four different structural zones which corresponds to three different type phases of deformation related to transitions in the rheology.

The frontal brittle part of the wedge is characterized by an imbricated zone and active in-sequence thrusts faults ahead. The décollement and the above sequence behave plastically (Figure 9a). The topographic slope created in this section is controlled by the basal and average internal frictions and is consistent with the CTT predictions (Figure 9b and c, blue star).

The presence of a smectite-illite transition (dehydration reaction) leads to a segment characterized by a flat topographic slope and little internal deformation, in between the frontal brittle wedge and the brittle-ductile transition (Figure 9a). This flat segment appears during the early stage of the accretionary prism formation. As the wedge shortens and grows, the temperature increases at the back due to burial and the wedge becomes thicker and warmer, reducing this frontal flat segment.

The brittle-viscous transition zone is characterized by out-of-sequence thrusts and backthrusts with high internal deformation (Figure 9a). This part forms a steeper topography slope than the brittle part. A careful examination of the behavior of this segment reveals that the décollement remains brittle, but the above sequence has entered the viscous phase (Figure 9a). By plotting the surface slope on the critical taper diagram, we notice that this part is consistent with a critical taper of a lower internal friction angle (Figure 9b, red star).

The viscous part presents an approximate flat zone without effective internal deformation. Décollement and above sequence deform viscously. The topographic slope is again consistent with the critical taper theory, considering that a viscous décollement is equivalent to a brittle décollement of extremely low friction. Therefore, the increase of the topographic slope between the brittle and viscous segments results from an equivalent decrease of internal friction rather than an increase of basal friction.

4.2 Comparison with exhumed accretionary prism

Based on the models, we can interpret that the rocks exhumed at the back of the models have been through 3 main phases of deformation through time. The first phase D1 is purely brittle and corresponds to the onset of accretion at the toe of the accretionary prism. The passive transport through the dehydration flat segment does not cause important deformation. D1 is therefore overprinted by a phase D2, which corresponds to the start development of a low grade metamorphic foliation as a result of penetrative horizontal shortening. This change in material behavior at depth, from brittle to viscous, due to an increase of temperature at depth, favors the activation of brittle backthrusts and causes the steepening of the slope. In an accretionary prism with large basal heat flow, or thick incoming sedimentary, the sequence D2 appears closer to the toe of the prism and might replace D1. Warmer models then develop a phase in which deformation is partitioned between ductile simple shear at depth (D3) and distributed shortening at the surface (more penetrative version of D2). Once the horizontal ductile shear zone corresponding to D3 has formed, it branches on a shallow dipping splay fault accompanied by a very vertical back-thrust. The

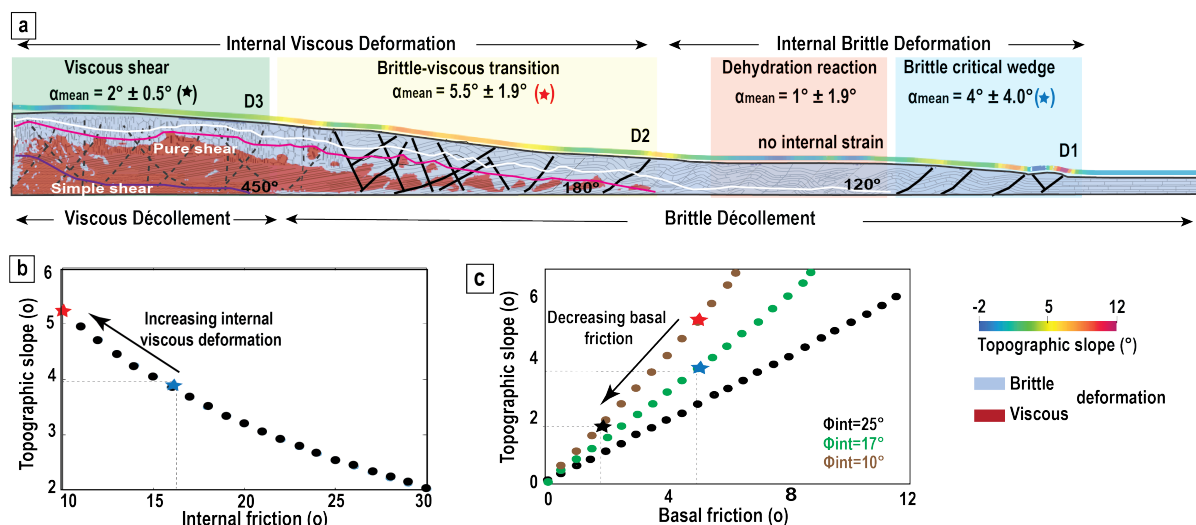


Figure 9. a. Proposed model for the mature brittle ductile wedge which forms three distinct segments; pure brittle wedge with a rather constant slope predicted by the CTT at the front (blue star), low but non zero topographic slope close to the backstop corresponds to viscous deformation (black star) and, larger topographic slope in between these segments as a result of the brittle ductile transition (red star and yellow rectangle). b. Topographic slope versus internal friction for $\phi_{\text{basal}} = 5^\circ$. c. Basal friction versus topographic slope for $\phi_{\text{int}} = 10, 17$ and 25° .

three phases of deformation recorded by the rocks exhumed at the back of the models along a normal fault correspond to the different phases recorded in exhumed accretionary prism like the Shimanto Belt (Raimbourg et al., 2014), although this paper would classify our D1 and D2 as more or less localised deformation related to frontal accretion and in our case the high grade ductile foliation D3 would show a more marked asymmetry.

4.3 Forearc basins

Every phase of deformation is accompanied by different types of sedimentary basins. Indeed, while phase D1 is accompanied by piggy-back basins which length depends on the sedimentation rate (e.g., Figure 4), D2 is accompanied with the formation of trench slope basins discordant on the early piggy-back basins, and the onset of D3 pinpoints the start of activity of the splay fault and its back-thrust. These structures isolate the ductile part of the prism, where forearc sediments can accumulate within small basins in discordance on the sediments accreted during D1 and D2, from the brittle part of the prism. The splay fault and its conjugate high angle back-thrust serve as a current backstop for the brittle part before being incorporated into the ductile forearc part of the prism as accretion continues.

Backthrusting between the imbricated segment and forearc basins have been described along various accretionary margins of high sedimentation rate (Silver and Reed, 1988). Along the Sumatra subduction zone, well-known for its high sedimentation rate and high thermal gradient (Chlieh et al., 2008), the slope break predicted by our model is visible on seismic images of



northern (Chauhan et al., 2009) and southwestern (Singh et al., 2010) Sumatra, and a clear backthrust has been imaged down to
355 7 s (15 km) (Chauhan et al., 2009). Backthrusts have also been imaged along the Antilles subduction zone, in particular along
the Barbados region, again known for its high sedimentation rate psilver1988backthrusting, laigle2013along. A backthrust
is also well documented in New Zealand (Barnes and Nicol, 2004) but has been interpreted as resulting from a change in
basal friction. Noda (2016) reviews a number of other compressive accretional margins which all seem to develop an active
backthrust at the edge of the forearc basin like in our models.

360 However, most of these seismic studies place the splay fault and its back-thrust at the limit of the continental crust which
posits, in a way, a stable position through time, at least relative to the upper plate. In our simulations, the location of the splay
fault is given a more dynamic nature as it corresponds more or less to the 450°C isotherm (Figure 10a). This isotherm at 15 km
depth corresponds to greenschist facies metamorphic conditions. Using typical sediments composition, perplex software yields
typical continental crust seismic attributes with $5.5 > V_p > 5$ km/s and V_s 2.5 km/s. With volcanoclastic sediments, larger
365 velocities are expected for similar metamorphic conditions. As a result, seismic refraction investigation of active margin would
definitely identify this part of the models as a continental crust or former arc crust. Using the location of the splay fault in warm,
compressional accretionary contexts like Southern Sumatra (Figure 10b) and Lesser Antilles (Figure 10c), we propose that what
is typically interpreted as attenuated continental or arc crust could also well mark the location of the brittle-ductile transition.
According to our models, along with accretionary prisms of little seismic activity, the forearc basin should correlate with the
370 fully viscous domain at least along high sedimentation rate and high thermal gradient compressive accretionary margins.

4.4 Up and down-dip end of the seismogenic zone

We here confirm that the smectite-illite transition produces a flat segment that can explain, for young or cold accretionary
complexes, the observed correlation between deep-sea terraces or fore-arc basins with large subduction earthquakes (Song
and Simons, 2003; Wells et al., 2003). In such specific contexts, the flat segment would thus underline the up-dip limit of the
375 seismogenic zone. Along seismically active accretionary prisms, an increase of topographic slope and decrease in apparent
geodetic coupling are interpreted as the down-dip limit of the seismogenic zone (Cubas et al., 2013). In the first case, the rise in
topographic slope indicates an increase of effective basal friction which corresponds to the down-dip end of dominant seismic
slip (Cubas et al., 2013; Pajang et al., 2021). In the second case, geodetic deformation at velocities that differs from subducting
plate velocities is generally interpreted as a lack of coupling on the plate interface based on elastic models (Perfettini et al.,
380 2010; Chlieh et al., 2008). Here we show that the brittle-ductile transition corresponds to the onset of internal distributed
viscous deformation in between brittle structures in the accretionary prism above a brittle décollement. This causes a decreased
geodetic coupling and an increased apparent basal friction but does not imply any modification in the interface frictional
properties or deformation mode. This questions both the search for field analogs of the down-dip end of the seismogenic zone
and the interpretation of seismic coupling in terms of locked/creeping décollement.

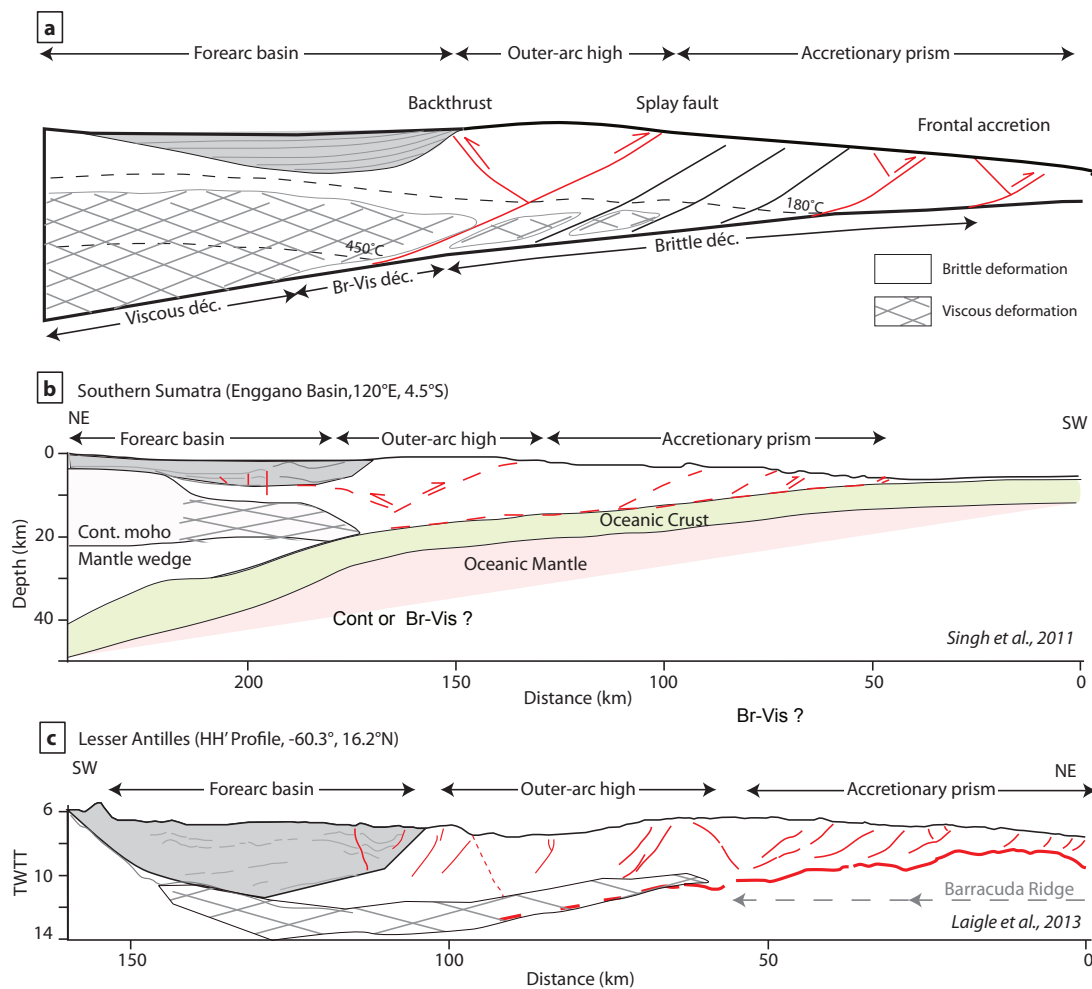


Figure 10. a. Structure of accretionary wedge and forearc basin modified from Noda (2016) based on our modelling results for the geometry of isotherms and the distribution of brittle and viscous strain. Schematic cross-sections of **b.** Southern Sumatra based on Singh et al. (2011) **c.** Lesser antilles based on Laigle et al. (2013) with indication of the possible location of the brittle ductile transition based on our model and the observed geometry of faults.



385 4.5 Limitations and perspectives

Our simple models permit us to understand first order mechanisms in forearc formation, but improvements are still needed to better understand how the brittle-ductile transition affects the formation of splay faults providing an alternative model to the formation of forearc basins as well as an alternative origin for the forearc crust. We find that, the drop in friction between the ductile and brittle part of the accretionary prism and smectite to illite dehydration reaction is not sufficient to explain the normal faults observed along some accretionary margins like Chile or Makran Cubas et al. (2013); Pajang et al. (2021). This result leads us to conclude that the normal faults arise from phenomena we neglected in our simplified approach. This includes:

- the effect of heterogeneities in the subducting plate,
- the effect of elastic deformation during the seismic cycle and/or
- the over simplification of the bottom boundary conditions which does not allow an increase in taper angle with burial like in Beaumont et al. (1992); Ruh (2020).

We plan on testing these other hypotheses in the future and posit that improving the bottom mechanical boundary conditions will also permit performing more accurate simulations of the sedimentation in the forearc basins by keeping them below sea level.

5 Conclusions

Despite the simplicity and limitations of our simulations, their results are sufficient to propose a new model for the interpretation of changes in topographic slope at compressive accretionary margins, at least, warm margins with large sedimentary supply. Using only the topographic gradient, our model distinguished four segments, which corresponds to 3 modes of deformations observed in exhumed accretionary complexes:

- brittle décollement and internal deformation at the toe where the topographic slope respects the CTT;
- a flat area with little internal deformation in young accretionary prisms, if a dehydration reaction is considered;
- brittle décollement and viscous internal deformation of fault-bounded blocks, where the topographic slope is in excess compared to the CTT and these large slopes should not be interpreted as the downdip limit of the seismogenic zone;
- viscous décollement and backthrust bounded blocks in the most internal part where the topographic slope is close to zero.

The most important finding is that the onset of internal viscous deformation in fault-bounded blocks increases the topographic slope of the accretionary complex independently of the basal friction.

Comparing the simulations results with natural cases, we show that this anomalous topography related to the brittle-ductile transition is analogue to the forearc high in a compressional accretionary prism. It is indeed the location of an active back-thrust and splay fault system rooting on the viscous channel that forms in the internal part where the basal temperature reaches



415 450°C . The location of this viscous channel, which is active in greenschist facies conditions, corresponds to portions of seismic sections that are often interpreted as an attenuated continental crust or former arc crust. Our model provides, we believe, a valid alternative interpretation which has the advantage to explain why the forearc crust is always thinner than the continental crust on seismic sections but also why the warm subduction segments are representative of our mature stage simulation, such as South Sumatra or the Lesser Antilles are considered aseismic.

420 *Code availability.* The version of `ptatin2d` and the input files used in this contribution are archived following FAIR principle at <https://doi.org/10.5281/zenodo.4911354>. Input files are located in `published_inputs/Pajang2021_SE`

Video supplement. all simulations are available as movies archived at <https://doi.org/10.5281/zenodo.5599365>

Author contributions. SP Designed the simulation, run the simulation prepared the figure and wrote the paper, LLP implemented the heat flow bc, LLP and NC, participated to the interpretation of the simulation, application to natural cases and writing the paper

425 .

Competing interests. Authors declare no competing interest

Acknowledgements. Authors thanks Tiphaine Larvet for computing seismic velocity with `perplex`.



References

- Barnes, P. M. and Nicol, A.: Formation of an active thrust triangle zone associated with structural inversion in a subduction setting, eastern
430 New Zealand, *Tectonics*, 23, 2004.
- Beaumont, C., Fullsack, P., and Hamilton, J.: Erosional control of active compressional orogens, in: *Thrust tectonics*, pp. 1–18, Springer, 1992.
- Bekins, B., McCaffrey, A. M., and Dreiss, S. J.: Influence of kinetics on the smectite to illite transition in the Barbados accretionary prism, *Journal of Geophysical Research: Solid Earth*, 99, 18 147–18 158, 1994.
- 435 Bonini, M.: Deformation patterns and structural vergence in brittle–ductile thrust wedges: an additional analogue modelling perspective, *Journal of Structural Geology*, 29, 141–158, 2007.
- Bonnet, C., Malavieille, J., and Mosar, J.: Interactions between tectonics, erosion, and sedimentation during the recent evolution of the Alpine orogen: Analogue modeling insights, *Tectonics*, 26, 2007.
- Borderie, S., Graveleau, F., Witt, C., and Vendeville, B. C.: Impact of an interbedded viscous décollement on the structural and kinematic
440 coupling in fold-and-thrust belts: Insights from analogue modeling, *Tectonophysics*, 722, 118–137, 2018.
- Braun, J. and Yamato, P.: Structural evolution of a three-dimensional, finite-width crustal wedge, *Tectonophysics*, 484, 181–192, 2010.
- Buiter, S. J., Schreurs, G., Albertz, M., Gerya, T. V., Kaus, B., Landry, W., Le Pourhiet, L., Mishin, Y., Egholm, D. L., Cooke, M., et al.: Benchmarking numerical models of brittle thrust wedges, *Journal of Structural Geology*, 92, 140–177, 2016.
- Burbidge, D. R. and Braun, J.: Numerical models of the evolution of accretionary wedges and fold-and-thrust belts using the distinct-element
445 method, *Geophysical Journal International*, 148, 542–561, 2002.
- Byerlee, J.: Friction of rocks, in: *Rock friction and earthquake prediction*, pp. 615–626, Springer, 1978.
- Chauhan, A. P., Singh, S. C., Hananto, N. D., Carton, H., Klingelhoefer, F., Dessa, J.-X., Permana, H., White, N., Graindorge, D., and Team, S. S.: Seismic imaging of forearc backthrusts at northern Sumatra subduction zone, *Geophysical Journal International*, 179, 1772–1780, 2009.
- 450 Chen, C.-T., Chan, Y.-C., Lo, C.-H., Malavieille, J., Lu, C.-Y., Tang, J.-T., and Lee, Y.-H.: Basal accretion, a major mechanism for mountain building in Taiwan revealed in rock thermal history, *Journal of Asian Earth Sciences*, 152, 80–90, 2018.
- Chlieh, M., Avouac, J.-P., Sieh, K., Natawidjaja, D. H., and Galetzka, J.: Heterogeneous coupling of the Sumatran megathrust constrained by geodetic and paleogeodetic measurements, *Journal of Geophysical Research: Solid Earth*, 113, 2008.
- Colletta, B., Letouzey, J., Pinedo, R., Ballard, J. F., and Balé, P.: Computerized X-ray tomography analysis of sandbox models: Examples of
455 thin-skinned thrust systems, *Geology*, 19, 1063–1067, 1991.
- Costa, E. and Vendeville, B.: Experimental insights on the geometry and kinematics of fold-and-thrust belts above weak, viscous evaporitic décollement, *Journal of Structural Geology*, 24, 1729–1739, 2002.
- Couzens-Schultz, B. A., Vendeville, B. C., and Wiltschko, D. V.: Duplex style and triangle zone formation: insights from physical modeling, *Journal of Structural Geology*, 25, 1623–1644, 2003.
- 460 Cubas, N., Leroy, Y., and Maillot, B.: Prediction of thrusting sequences in accretionary wedges, *Journal of Geophysical Research: Solid Earth*, 113, 2008.
- Cubas, N., Avouac, J.-P., Souloumiac, P., and Leroy, Y.: Megathrust friction determined from mechanical analysis of the forearc in the Maule earthquake area, *Earth and Planetary Science Letters*, 381, 92–103, 2013.



- 465 Dahlen, F., Suppe, J., and Davis, D.: Mechanics of fold-and-thrust belts and accretionary wedges: Cohesive Coulomb theory, *Journal of Geophysical Research: Solid Earth*, 89, 10087–10 101, 1984.
- Davis, D., Suppe, J., and Dahlen, F.: Mechanics of fold-and-thrust belts and accretionary wedges, *Journal of Geophysical Research: Solid Earth*, 88, 1153–1172, 1983.
- Fillon, C., Huismans, R. S., and van der Beek, P.: Syntectonic sedimentation effects on the growth of fold-and-thrust belts, *Geology*, 41, 83–86, 2013.
- 470 Fuller, C., Willett, S., Fisher, D., and Lu, C.: A thermomechanical wedge model of Taiwan constrained by fission-track thermochronometry, *Tectonophysics*, 425, 1–24, 2006.
- Gao, X. and Wang, K.: Strength of stick-slip and creeping subduction megathrusts from heat flow observations, *Science*, 345, 1038–1041, 2014.
- Graveleau, F., Malavieille, J., and Dominguez, S.: Experimental modelling of orogenic wedges: A review, *Tectonophysics*, 538, 1–66, 2012.
- 475 Gutscher, M.-A., Klaeschen, D., Flueh, E., and Malavieille, J.: Non-Coulomb wedges, wrong-way thrusting, and natural hazards in Cascadia, *Geology*, 29, 379–382, 2001.
- Hoth, S., Adam, J., Kukowski, N., and Oncken, O.: Influence of erosion on the kinematics of bivergent orogens: results from scaled sandbox simulations, *Tectonics, Climate, and Landscape Evolution*, 398, 201, 2006.
- Hyndman, R., Wang, K., and Yamano, M.: Thermal constraints on the seismogenic portion of the southwestern Japan subduction thrust, 480 *Journal of Geophysical Research: Solid Earth*, 100, 15 373–15 392, 1995.
- Jeffreys, H.: The Thermal Effects of Blanketing by Sediments., *Geophysical Journal International*, 2, 323–329, 1931.
- Jourdon, A., Le Pourhiet, L., Petit, C., and Rolland, Y.: Impact of range-parallel sediment transport on 2D thermo-mechanical models of mountain belts: Application to the Kyrgyz Tien Shan, *Terra Nova*, 30, 279–288, 2018.
- Konstantinovskaya, E. and Malavieille, J.: Accretionary orogens: erosion and exhumation, *Geotectonics*, 39, 69–86, 2005.
- 485 Koyi, H. A. and Vendeville, B. C.: The effect of décollement dip on geometry and kinematics of model accretionary wedges, *Journal of Structural Geology*, 25, 1445–1450, 2003.
- Lachenbruch, A. H. and Sass, J.: Heat flow and energetics of the San Andreas fault zone, *Journal of Geophysical Research: Solid Earth*, 85, 6185–6222, 1980.
- Laigle, M., Becel, A., De Voogd, B., Sachpazi, M., Bayrakci, G., Lebrun, J.-F., Evain, M., et al.: Along-arc segmentation and interaction of 490 subducting ridges with the Lesser Antilles Subduction forearc crust revealed by MCS imaging, *Tectonophysics*, 603, 32–54, 2013.
- Lallemand, S. E., Schnürle, P., and Malavieille, J.: Coulomb theory applied to accretionary and nonaccretionary wedges: Possible causes for tectonic erosion and/or frontal accretion, *Journal of Geophysical Research: Solid Earth*, 99, 12 033–12 055, 1994.
- Lanson, B., Sakharov, B. A., Claret, F., and Drits, V. A.: Diagenetic smectite-to-illite transition in clay-rich sediments: A reappraisal of X-ray diffraction results using the multi-specimen method, *American Journal of Science*, 309, 476–516, 2009.
- 495 Leturmy, P., Mugnier, J., Vinour, P., Baby, P., Colletta, B., and Chabron, E.: Piggyback basin development above a thin-skinned thrust belt with two detachment levels as a function of interactions between tectonic and superficial mass transfer: the case of the Subandean Zone (Bolivia), *Tectonophysics*, 320, 45–67, 2000.
- Lo, C.-H. and Onstott, T. C.: Rejuvenation of KAr systems for minerals in the Taiwan Mountain Belt, *Earth and Planetary Science Letters*, 131, 71–98, 1995.
- 500 Mandal, N., Chattopadhyay, A., and Bose, S.: Imbricate thrust spacing: experimental and theoretical analyses, in: *Evolution of geological structures in micro-to macro-scales*, pp. 143–165, Springer, 1997.



- Mary, B. C., Maillot, B., and Leroy, Y. M.: Predicting orogenic wedge styles as a function of analogue erosion law and material softening, *Geochemistry, Geophysics, Geosystems*, 14, 4523–4543, 2013.
- Mase, C. W. and Smith, L.: Pore-fluid pressures and frictional heating on a fault surface, *Pure and Applied Geophysics*, 122, 583–607, 1984.
- 505 Mase, C. W. and Smith, L.: Effects of frictional heating on the thermal, hydrologic, and mechanical response of a fault, *Journal of Geophysical Research: Solid Earth*, 92, 6249–6272, 1987.
- May, D. A., Brown, J., and Le Pourhiet, L.: pTatin3D: High-performance methods for long-term lithospheric dynamics, in: SC'14: Proceedings of the International Conference for High Performance Computing, Networking, Storage and Analysis, pp. 274–284, IEEE, 2014.
- May, D. A., Brown, J., and Le Pourhiet, L.: A scalable, matrix-free multigrid preconditioner for finite element discretizations of heterogeneous
510 Stokes flow, *Computer methods in applied mechanics and engineering*, 290, 496–523, 2015.
- Miyakawa, A., Yamada, Y., and Matsuoka, T.: Effect of increased shear stress along a plate boundary fault on the formation of an out-of-sequence thrust and a break in surface slope within an accretionary wedge, based on numerical simulations, *Tectonophysics*, 484, 127–138, 2010.
- Moore, J. C. and Saffer, D.: Updip limit of the seismogenic zone beneath the accretionary prism of southwest Japan: An effect of diagenetic
515 to low-grade metamorphic processes and increasing effective stress, *Geology*, 29, 183–186, 2001.
- Morrow, C., Shi, L., and Byerlee, J.: Strain hardening and strength of clay-rich fault gouges, *Journal of Geophysical Research: Solid Earth*, 87, 6771–6780, 1982.
- Mulugeta, G.: Modelling the geometry of Coulomb thrust wedges, *Journal of Structural Geology*, 10, 847–859, 1988.
- Nieuwland, D., Leutscher, J., and Gast, J.: Wedge equilibrium in fold-and-thrust belts: prediction of out-of-sequence thrusting based on
520 sandbox experiments and natural examples, *Netherlands Journal of Geosciences*, 79, 81–91, 2000.
- Noda, A.: Forearc basins: Types, geometries, and relationships to subduction zone dynamics, *Bulletin*, 128, 879–895, 2016.
- Oleskevich, D., Hyndman, R., and Wang, K.: The updip and downdip limits to great subduction earthquakes: Thermal and structural models of Cascadia, south Alaska, SW Japan, and Chile, *Journal of Geophysical Research: Solid Earth*, 104, 14 965–14 991, 1999.
- Pajang, S., Cubas, N., Letouzey, J., Le Pourhiet, L., Seyedali, S., Fournier, M., Agard, P., Khatib, M. M., Heyhat, M., and Mokhtari, M.:
525 Seismic hazard of the western Makran subduction zone: insight from mechanical modelling and inferred frictional properties, *Earth and Planetary Science Letters*, 562, 116 789, 2021.
- Perfettini, H., Avouac, J.-P., Tavera, H., Kositsky, A., Nocquet, J.-M., Bondoux, F., Chlieh, M., Sladen, A., Audin, L., Farber, D. L., et al.: Seismic and aseismic slip on the Central Peru megathrust, *Nature*, 465, 78–81, 2010.
- Perron, P., Le Pourhiet, L., Guiraud, M., Vennin, E., Moretti, I., Portier, É., and Konaté, M.: Control of inherited accreted lithospheric
530 heterogeneity on the architecture and the low, long-term subsidence rate of intracratonic basins, *BSGF-Earth Sciences Bulletin*, 192, 15, 2021.
- Pichot, T. and Nalpas, T.: Influence of synkinematic sedimentation in a thrust system with two decollement levels; analogue modelling, *Tectonophysics*, 473, 466–475, 2009.
- Pytte, A. and Reynolds, R.: The thermal transformation of smectite to illite. Pp. 133–140 in: *Thermal History of Sedimentary Basins (ND Naeser and TH McCulloh, editors)*, 1988.
- Raimbourg, H., Augier, R., Famin, V., Gadenne, L., Palazzin, G., Yamaguchi, A., and Kimura, G.: Long-term evolution of an accretionary prism: The case study of the Shimanto Belt, Kyushu, Japan, *Tectonics*, 33, 936–959, 2014.
- Ranalli, G. and Murphy, D. C.: Rheological stratification of the lithosphere, *Tectonophysics*, 132, 281–295, 1987.
- Ruh, J. B.: Submarine landslides caused by seamounts entering accretionary wedge systems, *Terra Nova*, 28, 163–170, 2016.



- 540 Ruh, J. B.: Numerical modeling of tectonic underplating in accretionary wedge systems, *Geosphere*, 16, 1385–1407, 2020.
- Ruh, J. B., Kaus, B. J., and Burg, J.-P.: Numerical investigation of deformation mechanics in fold-and-thrust belts: Influence of rheology of single and multiple décollements, *Tectonics*, 31, 2012.
- Ruh, J. B., Gerya, T., and Burg, J.-P.: High-resolution 3D numerical modeling of thrust wedges: Influence of décollement strength on transfer zones, *Geochemistry, Geophysics, Geosystems*, 14, 1131–1155, 2013.
- 545 Ruh, J. B., Gerya, T., and Burg, J.-P.: 3D effects of strain vs. velocity weakening on deformation patterns in accretionary wedges, *Tectonophysics*, 615, 122–141, 2014.
- Ruh, J. B., Sallarès, V., Ranero, C. R., and Gerya, T.: Crustal deformation dynamics and stress evolution during seamount subduction: High-resolution 3-D numerical modeling, *Journal of Geophysical Research: Solid Earth*, 121, 6880–6902, 2016.
- Saffer, D. M. and Marone, C.: Comparison of smectite-and illite-rich gouge frictional properties: application to the updip limit of the seismicogenic zone along subduction megathrusts, *Earth and Planetary Science Letters*, 215, 219–235, 2003.
- 550 Segall, P. and Rice, J. R.: Does shear heating of pore fluid contribute to earthquake nucleation?, *Journal of Geophysical Research: Solid Earth*, 111, 2006.
- Shea, W. T. and Kronenberg, A. K.: Rheology and deformation mechanisms of an isotropic mica schist, *Journal of Geophysical Research: Solid Earth*, 97, 15 201–15 237, 1992.
- 555 Sibson, R.: Interactions between temperature and pore-fluid pressure during earthquake faulting and a mechanism for partial or total stress relief, *Nature Physical Science*, 243, 66–68, 1973.
- Silver, E. A. and Reed, D. L.: Backthrusting in accretionary wedges, *Journal of Geophysical Research: Solid Earth*, 93, 3116–3126, 1988.
- Simpson, G.: Mechanics of non-critical fold–thrust belts based on finite element models, *Tectonophysics*, 499, 142–155, 2011.
- Simpson, G. D.: Modelling interactions between fold–thrust belt deformation, foreland flexure and surface mass transport, *Basin Research*, 18, 125–143, 2006.
- 560 Simpson, M. J., Landman, K. A., and Hughes, B. D.: Cell invasion with proliferation mechanisms motivated by time-lapse data, *Physica A: Statistical Mechanics and its Applications*, 389, 3779–3790, 2010.
- Singh, S. C., Hananto, N. D., Chauhan, A. P., Permana, H., Denolle, M., Hendriyana, A., and Natawidjaja, D.: Evidence of active backthrusting at the NE Margin of Mentawai Islands, SW Sumatra, *Geophysical Journal International*, 180, 703–714, 2010.
- 565 Singh, S. C., Hananto, N., Mukti, M., Robinson, D. P., Das, S., Chauhan, A., Carton, H., Gratacos, B., Midnet, S., Djajadihardja, Y., et al.: Aseismic zone and earthquake segmentation associated with a deep subducted seamount in Sumatra, *Nature Geoscience*, 4, 308–311, 2011.
- Smit, J., Brun, J., and Sokoutis, D.: Deformation of brittle-ductile thrust wedges in experiments and nature, *Journal of Geophysical Research: Solid Earth*, 108, 2003.
- 570 Song, T.-R. A. and Simons, M.: Large trench-parallel gravity variations predict seismogenic behavior in subduction zones, *Science*, 301, 630–633, 2003.
- Stockmal, G. S., Beaumont, C., Nguyen, M., Lee, B., and Sears, J.: Mechanics of thin-skinned fold-and-thrust belts: Insights from numerical models, *SPECIAL PAPERS-GEOLOGICAL SOCIETY OF AMERICA*, 433, 63, 2007.
- Storti, F. and McClay, K.: Influence of syntectonic sedimentation on thrust wedges in analogue models, *Geology*, 23, 999–1002, 1995.
- 575 Strayer, L. M., Hudleston, P. J., and Lorig, L. J.: A numerical model of deformation and fluid-flow in an evolving thrust wedge, *Tectonophysics*, 335, 121–145, 2001.
- Suppe, J. et al.: Mechanics of mountain building and metamorphism in Taiwan, *Mem. Geol. Soc. China*, 4, 67–89, 1981.



- Terzaghi, K.: Erdbaumechanik auf bodenphysikalischer Grundlage, F. Deuticke, 1925.
- Vrolijk, P.: On the mechanical role of smectite in subduction zones, *Geology*, 18, 703–707, 1990.
- 580 Wangen, M.: The blanketing effect in sedimentary basins, *Basin Research*, 7, 283–298, 1994.
- Wells, R. E., Blakely, R. J., Sugiyama, Y., Scholl, D. W., and Dinterman, P. A.: Basin-centered asperities in great subduction zone earthquakes: A link between slip, subsidence, and subduction erosion?, *Journal of Geophysical Research: Solid Earth*, 108, 2003.
- Willett, S. D.: Rheological dependence of extension in wedge models of convergent orogens, *Tectonophysics*, 305, 419–435, 1999.
- Willett, S. D. and Brandon, M. T.: On steady states in mountain belts, *Geology*, 30, 175–178, 2002.
- 585 Yamato, P., Kaus, B. J., Mouthereau, F., and Castelltort, S.: Dynamic constraints on the crustal-scale rheology of the Zagros fold belt, Iran, *Geology*, 39, 815–818, 2011.